RESEARCH

Sunlight Responsive 2D/2D SnS$_2$/BiVO$_4$ Nanocomposite for Photocatalytic Removal of Ciprofloxacin Antibiotic from Aqueous Medium

Gandharve Kumar[1]

Abstract

A bismuth vanadate (BiVO$_4$) irregular nanoplates surface decorated with tin disulphide (SnS$_2$) nanoplates is developed as a visible light responsive photocatalyst for the degradation of ciprofloxacin antibiotics. The photocatalyst, named SnS$_2$/BiVO$_4$ is characterized by various physiochemical techniques such as powder X-Ray diffraction, field-emission scanning electron microscopy, high-resolution transmission electron microscopy, X-ray photoelectron spectroscopy, UV–vis diffuse reflectance spectroscopy, electrochemical impedance spectroscopy and photoluminescence. The optimized batch 0.15SnS$_2$/BiVO$_4$ photocatalysts degraded 92% (CIP, 10 mg/L) with a rate constant 0.0184 min^{-1}, which was about 3.75 times and 7.66 times higher than that of the BiVO$_4$ ($k=0.0049$ min^{-1}) and SnS$_2$ ($k=0.0024$ min^{-1}) photocatalyst respectively. The improved photocatalytic performance of SnS$_2$/BiVO$_4$ nanocomposite is mainly due to (a) strengthened visible light absorption by 0.15SnS$_2$/BiVO$_4$ due to the shifting of absorption edge towards higher wavelength (b) Z-scheme-like band position of BiVO$_4$ and SnS$_2$, (c) efficient inhibition of charge carrier recombination, and (d) in situ generation of reactive oxygen species.

Graphical Abstract
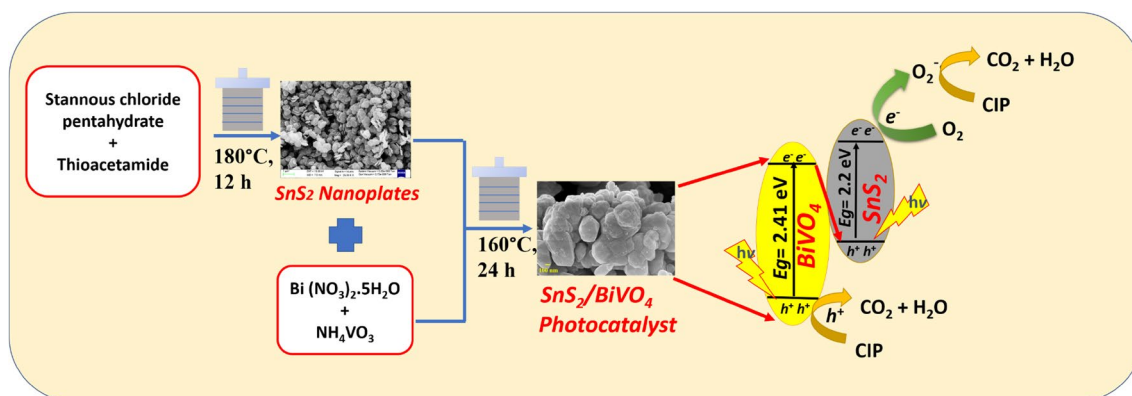
Keywords Z-scheme · SnS$_2$ · BiVO$_4$ · Solar photocatalyst · Antibiotics degradation.

1 Introduction

Harmful organic pollutants such as pharmaceutical products, personal care products, dyes, pesticides etc., released from the pharmaceutical, plastic, textile and leather industries into the water bodies are of great concern [1–4]. Ciprofloxacin drug is one of the broad-spectrum antibiotics, which have

✉ Gandharve Kumar
    gandhravk.engineering@tmu.ac.in

1   Department of Chemistry, Faculty of Engineering,
    Teerthanker Mahaveer University, Moradabad 244001, India

found wide applications in treating various bacterial infections in animals and humans [5–7]. Their consumption has been tremendously increased worldwide because of their low cost [8]. However, the long persistent nature of these drugs due to their slow metabolized nature in an aqueous medium, make them fatal for the water bodies [9, 10]. They can easily toxify ground and surface water, causing harmful infection in animals and humans due to the development of anti-bacterial resistant strains inside their bodies [11, 12]. Many techniques have been used to date, out of which semiconductor-based photocatalysis has found great potential in removing antibiotics from wastewater [8, 13, 14]. However, majority of the semiconductor photocatalysts suffered from certain limitations such as high charge carrier recombination rate, low redox properties, intrinsic defects, etc. [15–17]. Therefore, it is of great interest to design an efficient visible light active photocatalyst with high stability and enhanced photocatalytic activity toward the antibiotic degradation in an aqueous medium under sunlight irradiation.

Bismuth vanadate ($BiVO_4$) is the simplest ternary oxide semiconductor, with monoclinic scheelite phase. Due to its unique structure, together with its non-toxic, environmentally benign nature with excellent chemical stability, $BiVO_4$ has been considered a promising material for photocatalytic applications [18–20]. As compared with large band gap TiO_2 whose electronic structure consists of only O 2p orbitals, the $BiVO_4$ consists of Bi 6s and O 2p orbitals, the presence of extra Bi 6s orbital minimize the distance of excited electron from the valence band of $BiVO_4$ to the conduction band of V3d state of VO_4^{3-}, which results in the reduction of band gap energy, therefore increasing the light absorption region up to visible light [21, 22]. However, the low band gap (2.4–2.5 eV) makes $BiVO_4$ susceptible to rapid recombination of the photoexcited charge carriers, and thus, various strategies have been designed to overcome the intrinsic limitations of pristine $BiVO_4$ [23–25]. For instance, the construction of Z-scheme type heterojunctions with semiconductors having matching band edges with respect to that of $BiVO_4$ has proven to be an effective approach to overcome these limitations [26, 27]. The construction of a Z-scheme heterojunction composite is beneficial from a photocatalytic point of view by minimizing the charge carrier recombination rate and possessing strong redox abilities [28–30]. This occurs due to the retention of electron and holes in thermodynamic favorable condition i.e., electrons in the conduction band of one semiconductor and holes in the valence band of other in the heterostructure, which then takes part in the redox reactions generating in-situ active species required for the photocatalytic process [31–33]. Yong et al. prepared a Z-scheme $In_2S_3/BiVO_4$ photocatalyst, which shows enhanced photocatalytic activity towards the degradation of glyphosate [26]. Luo et al. synthesized a $MoSe_2/BiVO_4$ heterojunction with Z-scheme, which exhibits superior photocatalytic performance toward the photocatalytic removal of glyphosate [34]. Similarly, Chen et al. prepared Z-scheme $AgI/BiVO_4$ heterojunction which show superior photocatalytic activity toward the degradation of tetracycline under visible light irradiation [35].

In this regard, the band edges of a small band gap semiconductor, SnS_2, match well with that of $BiVO_4$, and hence, using SnS_2 as a sensitizer to construct heterostructure with $BiVO_4$ can improve the photocatalytic performance of the photocatalyst [26, 36]. In this work, a novel $SnS_2/BiVO_4$ heterostructure was fabricated via a two-step hydrothermal route. The effects of varying mass ratios of SnS_2 and $BiVO_4$ on the physicochemical properties of the as-synthesized composites were analysed by their structural, morphological, and optical properties. A possible formation of a Z-scheme heterostructure between $BiVO_4$ and SnS_2 has been proposed. The $SnS_2/BiVO_4$ nanocomposite exhibited enhanced photocatalytic efficiency towards ciprofloxacin (CIP) degradation under natural sunlight.

2 Experimental Section

2.1 Preparation of SnS_2

Firstly, SnS_2 nanoplates were synthesized using the hydrothermal method. stannous chloride pentahydrate (4mmol), thioacetamide (12 mmol), were dispersed in 70 mL DI water. The final suspension was transferred to a Teflon-lined stainless autoclave (100 mL) and maintained at 180 °C for 12 h in an oven. Finally, the supernatant liquid was discarded, and the final product was collected, washed with water and ethanol, and dried at 50 °C overnight.

2.2 Preparation of $SnS_2/BiVO_4$

The $SnS_2/BiVO_4$ nanocomposites were prepared by a hydrothermal method. 2 mmol NH_4VO_3, and 2 mmol $Bi(NO_3)_3 \cdot 5H_2O$ were mixed in 50 mL DI water under stirring for 30 min. The pH of the reaction mixture was kept at about 5–6 using NaOH (10.0 M) solutions. Afterward, the specified amount of SnS_2 (wt%) (10 wt%, 15 wt%, and 20 wt%) was added to the above reaction mixture under constant stirring. Finally, the resulting solution was transferred into a Teflon-lined autoclave and kept at 160 °C for 24 h. The obtained batches of $SnS_2/BiVO_4$ nanocomposites were centrifuged and washed with water and ethanol several times and dried at 60 °C overnight. The batches of $SnS_2/BiVO_4$ nanocomposites were denoted as $0.10SnS_2/BiVO_4$, $0.15SnS_2/BiVO_4$, and $0.20SnS_2/BiVO_4$ according to the amount of SnS_2 precursor added. The pure $BiVO_4$ was prepared by the same synthesis protocol without using SnS_2.

2.3 Characterization of Photocatalyst

The as-synthesized batches of $SnS_2/BiVO_4$ NCs, $BiVO_4$, and SnS_2 were characterized by different techniques. All details related to these techniques, including the sample preparation, were discussed in Section S1 of Supporting Information.

2.4 Photocatalytic Activity Test

The photocatalytic test of the $SnS_2/BiVO_4$ nanocomposites were conducted by degrading ciprofloxacin (CIP, 10 mg/L, 100 mL) using 0.06 g of photocatalyst in aqueous solution under the exposure of natural sunlight. Before the irradiation, the reaction mixtures were vigorously stirred for 60 min under dark to ensure adsorption/desorption equilibrium and then the reaction mixture were kept under natural sunlight for about 105 min in order to carry out the degradation studies. During photoreaction, 1 mL of aliquots was collected at regular intervals and centrifuged to separate the solid photocatalyst. Finally, the CIP concentration were monitored by UV–vis spectrophotometer. The leached concentrations of Bi, V, and Sn were analysed with the help of ICP-OES following the calibration technique (details were discussed in Supporting Information section S2).

3 Results and Discussion

3.1 XRD Analysis

The crystalline structure and phase composition of the as-synthesized heterostructures were analysed through XRD method, as represented in Fig. 1a. All the XRD peaks of $BiVO_4$ and SnS_2 are in good agreement with their monoclinic scheelite phase (JCPDS No.- 14-0688) and hexagonal phase (JCPDS No.-83-1705) respectively [37, 38]. The diffraction peak of the $SnS_2/BiVO_4$ heterojunction are similar to the $BiVO_4$, which confirm that the coupling of SnS_2 does not alter the phase of $BiVO_4$ (Fig. 1a). No distinctive peak of SnS_2 were observed in the $SnS_2/BiVO_4$ nanocomposite but in the enlarged view (Fig. 1b), reveals some shift in the peak at about 2θ of 29.1° and 30.7° related to the (121) and (040) lattice planes (Fig. 1b), when compared to $BiVO_4$, the XRD peaks of $SnS_2/BiVO_4$ shows slightly shift towards the higher 2θ region. This event suggested the strong interaction and intimate contact between SnS_2 and $BiVO_4$ [39]. The detailed information about the crystallite size of $SnS_2/BiVO_4$ NCs and $BiVO_4$ are discussed in supporting information section S3.

3.2 FE-SEM and HR-TEM Analysis

The microstructure and sizes of pure SnS_2, $BiVO_4$, and $0.15SnS_2/BiVO_4$ nanocomposites were investigated by field emission electron microscopy (FE-SEM) (Fig. 2). The FESEM image of SnS_2 reveals the formation of a nanoplates of irregular sizes having diameters of 150–250 nm (Fig. 2a). The FESEM image of $BiVO_4$ revealed a smooth irregular nanoplates-like structure with a size ranging between 300 and 700 nm in length (Fig. 2b). The FE-SEM image of $0.15SnS_2/BiVO_4$ reveals the formation of irregular nanoplates of $BiVO_4$ with nanoparticles of SnS_2 tightly adhered to the surface of $BiVO_4$ (Fig. 2c), which is substantiated from the XRD data also. Thus, it can be inferred that loading SnS_2 nanoplates on $BiVO_4$ irregular nanoplates surface favours charge transmission between the two components;
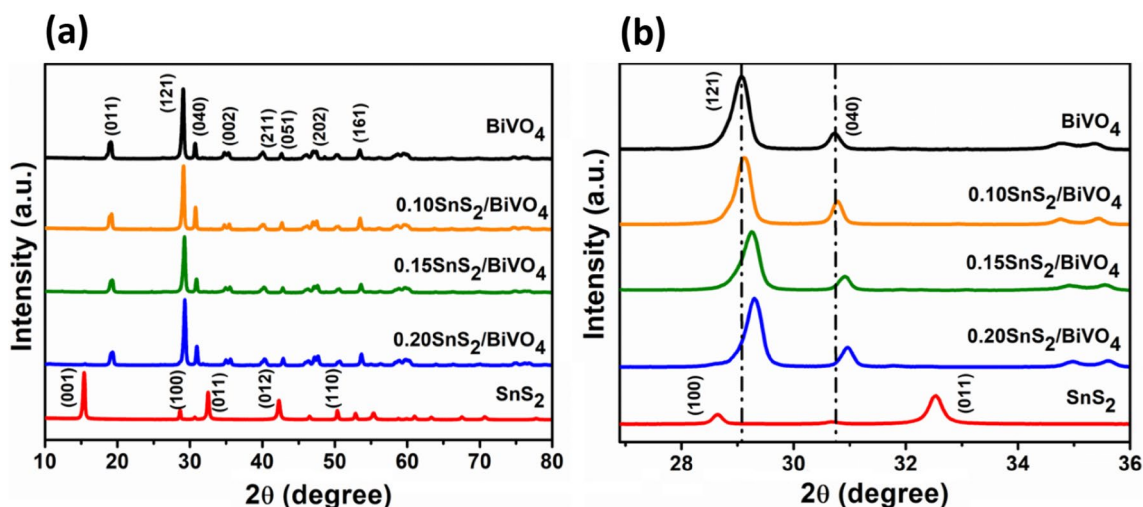

Fig. 1 **a** XRD pattern, **b** corresponding XRD pattern in the range 27°–36° of $BiVO_4$, SnS_2, and $SnS_2/BiVO_4$ nanocomposite
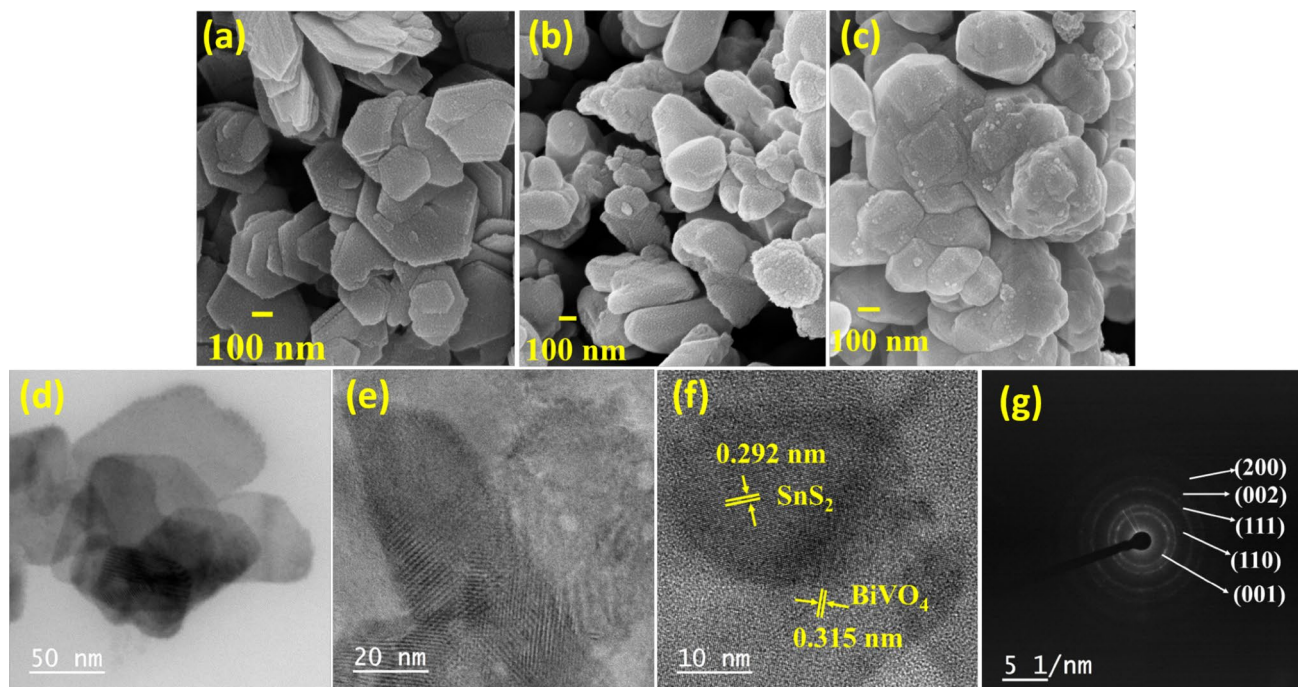
Fig. 2 FESEM image of (**a**) SnS_2; (**b**) $BiVO_4$; (**c**) $0.15SnS_2/BiVO_4$ nanocomposite; TEM images of $0.15SnS_2/BiVO_4$ (**d-e**); HR-TEM images of $0.15SnS_2/BiVO_4$ (**e**); and (**g**) SAED pattern of $0.15SnS_2/BiVO_4$

however, the $SnS_2/BiVO_4$ composites retain the morphology, size, and hierarchical structure of pristine $BiVO_4$.

The detailed morphology and microstructure of $0.15SnS_2/BiVO_4$ NCs were further investigated by HR-TEM, and it can be observed that the nanoplates of SnS_2 in the range of 80–100 nm were evenly dispersed over the 100–300 nm long nanoplates of $BiVO_4$ (Fig. 2d-e). As shown in Fig. 2f, the lattice fringe (0.315 nm) of $0.15SnS_2/BiVO_4$ corresponds to (121) plane of monoclinic $BiVO_4$, while the other interatomic layer spacing of (0.292 nm) corresponds to the (011) lattice phase of hexagonal SnS_2. The SAED pattern confirms the polycrystalline nature of $0.15SnS_2/BiVO_4$, and the obtained electron diffractions rings were indexed, which corresponds to the monoclinic phase of $BiVO_4$ (JCPDS No. 14-0688) (Fig. 2g).

3.3 XPS Analysis

XPS analysis was used to investigate the chemical composition of $0.15SnS_2/BiVO_4$, Fig. 3a exhibits the survey spectrum of batch $0.15SnS_2/BiVO_4$ nanocomposite and high-resolution XPS spectra of Bi $4f$, V $2p$, Sn$3d$, S $2p$, and O $1s$. The XPS spectra reveal that the $0.15SnS_2/BiVO_4$ nanocomposite consists of Bi, V, Sn, S, and O elements. The XPS spectrum of Bi $4f$ revealed two major peaks at 164.01 eV and 158.77 eV, which corresponds to Bi $4f_{5/2}$ and Bi $4f_{7/2}$, respectively (Fig. 3b). The XPS spectra of V $2p$ shows two peaks at 523.91 eV and 516.03 eV which corresponds to

V$2p_{1/2}$ and V$2p_{3/2}$, which represents vanadium (V) in the state of V^{5+} state as shown in Fig. 3c. The Sn^{4+} state in the $0.15SnS_2/BiVO_4$ photocatalyst is reflected from the peaks at 486.49 eV and 494.85 eV (Fig. 3d), which corresponded to Sn $3d_{5/2}$ and Sn $3d_{3/2}$ peaks, respectively. In the S $2p$ XPS spectra shows two peaks at 162.40 eV and 161.46 eV, which attributes to Sn$2p_{1/2}$ and Sn $2p_{3/2}$, respectively, that correspond to S^{2-} ion in SnS_2 (Fig. 3e). The O $1s$ spectra show peaks at 529.50 eV, which was related to crystal lattice oxygen in $0.15SnS_2/BiVO_4$ nanocomposite and at 530.02 eV which could possibly due to the surface defects and adsorbed oxygen species (Fig. 3f).

3.4 UV–Vis DRS Analysis

The optical properties of SnS_2, $BiVO_4$, and $SnS_2/BiVO_4$ were explored by UV–vis DRS spectra. Figure 4a reveals that pristine $BiVO_4$ and the $SnS_2/BiVO_4$ composites exhibit strong absorbance in the UV region extending to the visible light region, whereas SnS_2 absorbs only in the visible region (~570 nm) (inset of Fig. 4a). The absorption band edges of $BiVO_4$ lie at around 480 nm and on increasing the SnS_2 content, the absorption wavelength of the $SnS_2/BiVO_4$ composites exhibit a red shift with respect to pristine $BiVO_4$. Using the Tauc expression, $(\alpha h\nu)^{1/n} = A(h\nu - E_g)$ [40], the optical band gaps (E_g) of pristine $BiVO_4$, SnS_2, and $SnS_2/BiVO_4$ composites were calculated. Here α, h, ν, represent absorption coefficient,
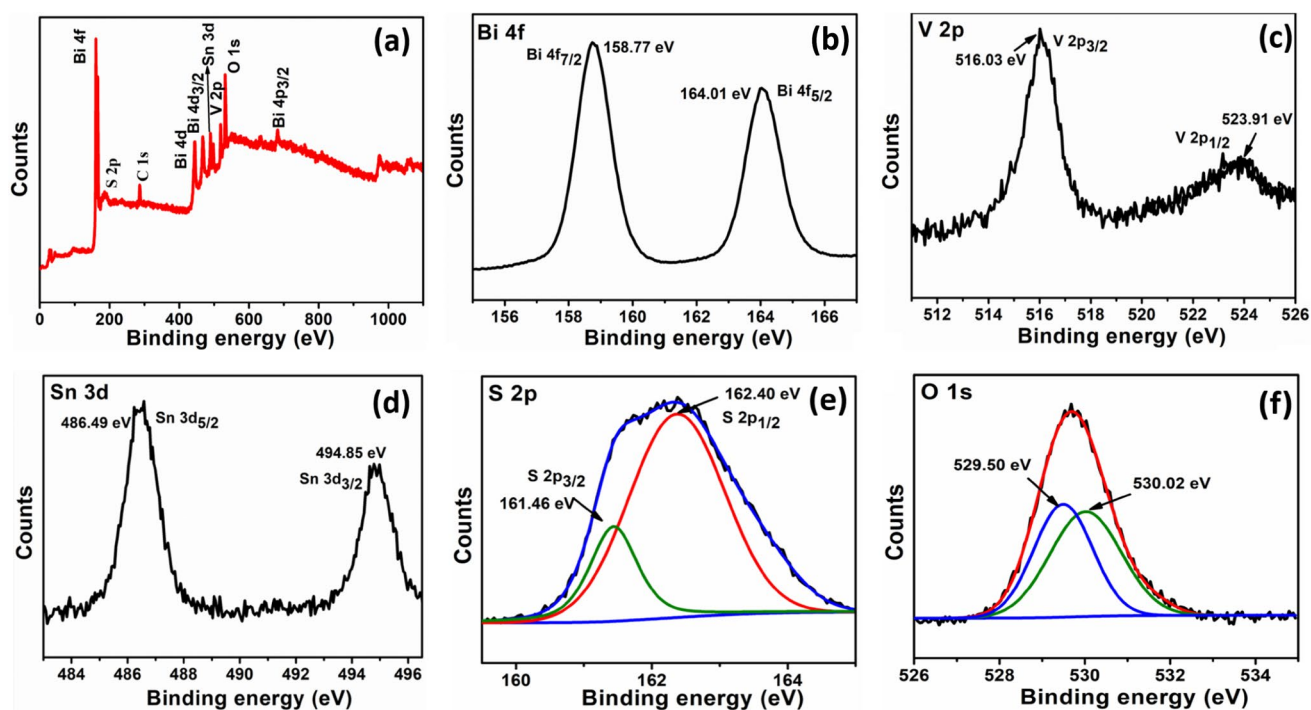
Fig. 3 XPS spectra of $0.15SnS_2/BiVO_4$ nanocomposite **a** survey spectra; **b** Bi $4f$; **c** V $2p$; **d** Sn $3d$; **e** S $2p$; and **f** O $1s$
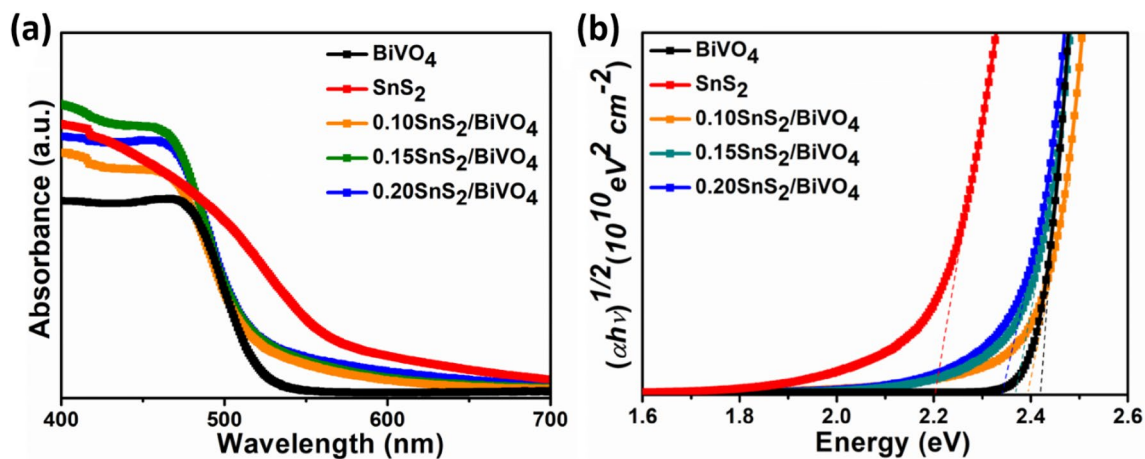

Fig. 4 **a** UV-DRS spectra of SnS_2, $BiVO_4$, and $SnS_2/BiVO_4$ nanocomposites, **b** Tauc's plot of SnS_2, $BiVO_4$, and $SnS_2/BiVO_4$.

Planck constant, irradiation frequency, whereas A, E_g and n represent the absorption constant, gap energy and a constant, respectively. Combining SnS_2 (E_g =2.2 eV) with $BiVO_4$ (E_g = 2.41 eV) results in a red shift in the values of the band gap to 2.39 eV, 2.36 eV and 2.34 eV for $0.10SnS_2/BiVO_4$, $0.15SnS_2/BiVO_4$, and $0.20SnS_2/BiVO_4$ composites respectively (Fig. 4b). Thus, it can be inferred that optical band-gaps of heterostructure composites can be finely tuned by regulating the weight ratios of the two semiconductors.

3.5 BET Analysis

The textural features of $BiVO_4$, SnS_2, and $0.15SnS_2/BiVO_4$ were determined from BET isotherm surface area and Barrett-Joyner-Halenda (BJH) pore size distribution curves and the results are presented in Fig. 5. All isotherm curves (Fig. 5a) are related to type-IV with H3 hysteresis. The specific surface area of $BiVO_4$, SnS_2, and $0.15SnS_2/BiVO_4$ are determined as21.2m^{2}g^{-1}, 51.4m^{2}g^{-1}, and34.6m^{2}g^{-1}, respectively, while their pore volumes are 0.02 cm^{3}g^{-1},
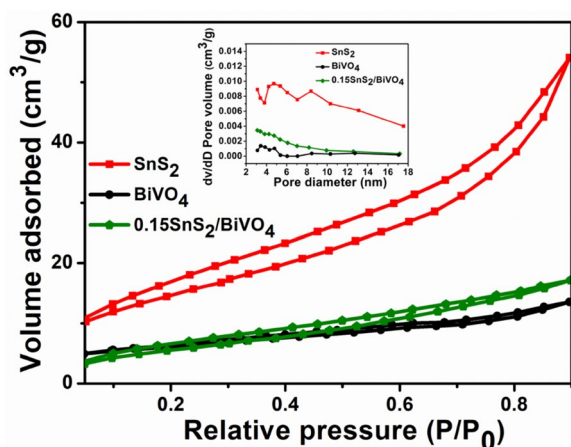
Fig. 5 Nitrogen adsorption-desorption isotherms and pore size distribution plots (inset) of SnS_2, $BiVO_4$, and $0.15SnS_2/BiVO_4$ NCs.

$0.12 \text{ cm}^3\text{g}^{-1}$, and $0.03 \text{ cm}^3\text{g}^{-1}$, respectively (Table. S2). The pore size distribution curves (Fig. 5b) show pore size distribution between 3 and 9 nm, which further substantiates its mesoporous characteristics. Compared to $BiVO_4$, the specific surface area and pore volume of $0.15SnS_2/BiVO_4$ is more, which is attributable to deposition of SnS_2 on the nanoplates of $BiVO_4$. Such mesoporous texture can be an advantage for improving its adsorptive photocatalytic efficiency.

3.6 Photocatalytic Measurement

The impact of photocatalyst dose on the photocatalytic performance was investigated by treating the aqueous solution CIP with different amounts of photocatalyst, i.e., 40–80 mg of photocatalyst per 100 mL under the same experimental environment as mentioned above. The degradation rate and removal efficiency were first increased with the increase in the photocatalyst dose from 0.4 mg/mL ($k = 0.0044 \text{ min}^{-1}$) to 0.6 mg/mL ($k = 0.0184 \text{ min}^{-1}$) and then decreased for the dose 0.8 mg/mL ($k = 0.0115 \text{ min}^{-1}$) (Fig.S1). The impact of the change in concentration of CIP solution has been investigated by changing the initial concentration of CIP solution from 10 to 30 mg/L. The decrease in the photocatalytic performance was observed with the increase in CIP concentrations from 10 mg/L ($k = 0.0184 \text{ min}^{-1}$) to 30 mg/L ($k = 0.0041 \text{ min}^{-1}$) (Fig.S1). A complete photocatalytic degradation study was performed with a photocatalyst dose of 60 mg per 100 mL aqueous solution of CIP (10 mg/L).

Photocatalytic degradation efficacies of pristine $BiVO_4$, SnS_2, and batches of $SnS_2/BiVO_4$ composites were tested against ciprofloxacin drug (10 mg/L^{-1}). The photocatalytic test was performed under natural sunlight. The degradation profile of CIP under sunlight irradiation by $SnS_2/BiVO_4$ NCs, $BiVO_4$ irregular nanoplates, and SnS_2 nanoplates

are showed in Fig. 6b. Ciprofloxacin shows negligible self-degradation without any catalyst, whereas the pristine SnS_2 and $BiVO_4$ displayed poor photocatalytic efficiency toward the CIP degradation after 105 min of sunlight irradiation. From all the batches prepared the optimized batch $0.15SnS_2/BiVO_4$ shows the highest photocatalytic degradation efficiency towards the CIP, which was about 92% after 105 min of sunlight irradiations. The degradation rate and removal efficiency were first increased with the increase in the amount of SnS_2 added from 0.10 wt% to 0.15 wt% in $SnS_2/BiVO_4$ NCs. The possible reason for this increase may be the better separation and transmission of photogenerated $e^- - h^+$ pairs. When the amount of SnS_2 is further increased from 0.15 wt% to 0.20 wt%, the active sites present on the $BiVO_4$ will be occupied, due to which the light absorption tendency has been reduced, leading to a decrease in photocatalytic efficiency.

Moreover, the degradation mechanism was estimated by fitting time-dependent CIP degradation data with a pseudo-first-order: $ln(C_0/C) = kt$, as shown in Fig. 6c, where C_0 is the initial concentration of CIP, C is the concentration at a preselected time t, and the k is apparent reaction rate constant (Table 1). The optimized batch $0.15SnS_2/BiVO_4$ exhibited the highest apparent rate constant ($k = 0.0184 \text{ min}^{-1}$), which is 3.75 and 7.66 times of $BiVO_4$ ($k = 0.0049 \text{ min}^{-1}$) and SnS_2 ($k = 0.0024 \text{ min}^{-1}$), respectively. Figure 6a shows the corresponding UV–vis absorption spectrum of CIP degraded by the optimized batch $0.15SnS_2/BiVO_4$ under sunlight irradiation. The decrease in the intensity of absorption peak of CIP (276 nm) was observed over 105 min period of sunlight irradiation.

3.7 Radical Trapping Experiment

To determine the involvement of *in-situ* generated ROS by $0.15SnS_2/BiVO_4$ heterojunction composite towards CIP degradation, specific ROS scavenging studies were performed. Various ROS scavengers like, chloroform (1mM) [41], ammonium oxalate (AO, 1mM) [42], and isopropyl alcohol (IPA 1mM) [43], were used as the quenchers for $O_2^{-\bullet}$, h^+, and $\bullet$OH radicals respectively (Fig. 6d). The photocatalytic performance of $0.15SnS_2/BiVO_4$ significantly decrease with the addition of chloroform, whereas similar observation was obtained after the addition of ammonium oxalate as a quencher. However, in case of IPA as a quencher slight considerable decrease in the degradation rate was observed, which indicate that superoxide anion radical ($O_2^{-\bullet}$) and hole (h^+) play more pivotal role than hydroxyl ($\bullet$OH) radicals in degradation process.

Apart from the excellent photocatalytic degradation performance, the re-usability, and leaching of the different metal species during the photocatalytic degradation were also playing a major role in the application. Figure 7a
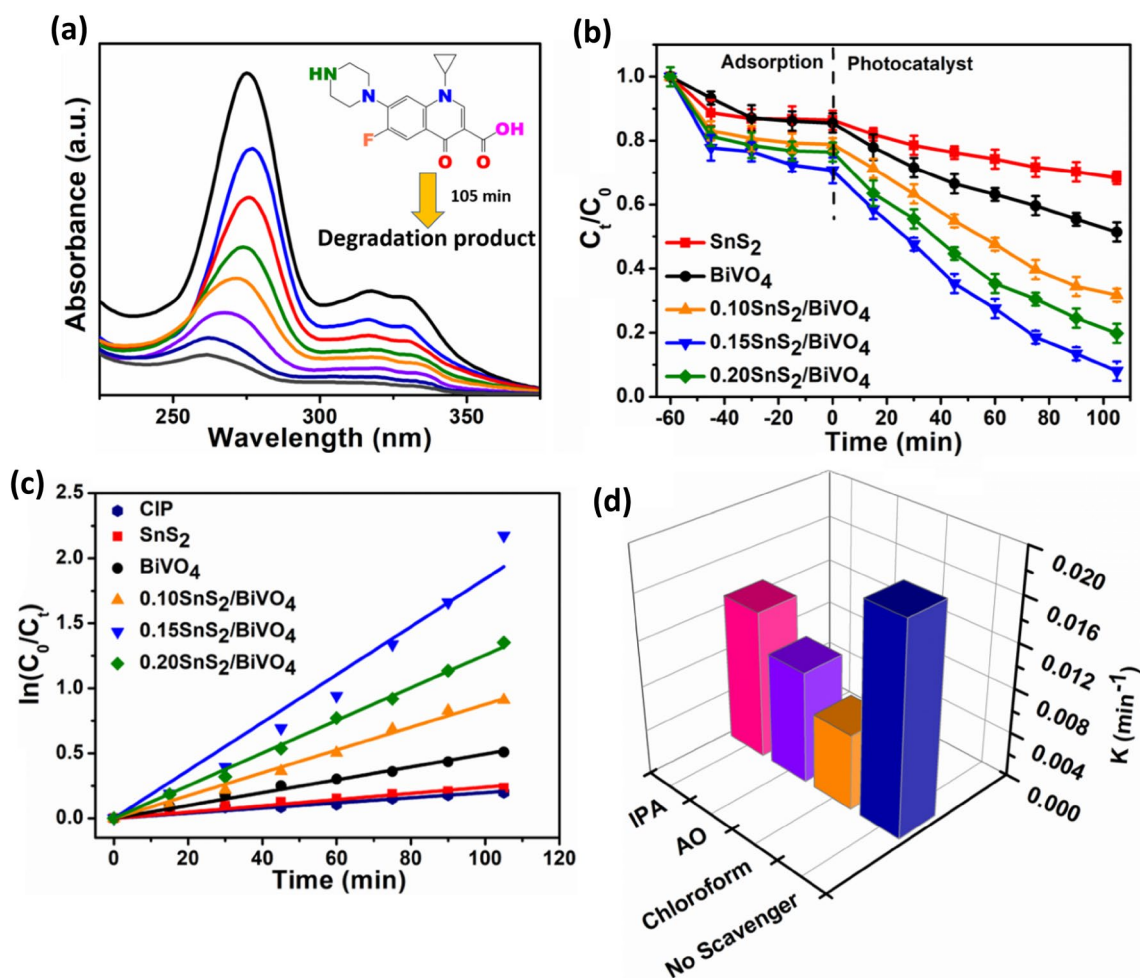
Fig. 6 (**a**) UV–vis absorption spectrum of CIP solution in presence of 0.15SnS$_2$/BiVO$_4$, (**b**) degradation plot of CIP by SnS$_2$, BiVO$_4$, and SnS$_2$/BiVO$_4$ nanocomposites, (**c**) corresponding pseudo-first-order kinetic plot, and, (**d**) radical trapping experiment for CIP over 0.15SnS$_2$/BiVO$_4$ photocatalyst

Table 1 Summary of the photocatalytic degradation experiments.

Sample name	Ads %	Deg %	First-order kinetics (CIP)	
			k (min^{-1})	R^2
0.20SnS$_2$/BiVO$_4$	24%	81%	0.0125	0.996
0.15SnS$_2$/BiVO$_4$	30%	92%	0.0184	0.991
0.10SnS$_2$/BiVO$_4$	22%	69%	0.0087	0.994
BiVO$_4$	15%	49%	0.0049	0.993
SnS$_2$	14%	32%	0.0024	0.995
Blank	NA	10%	0.0010	0.986

NA: Not Applicable

shows the re-usability of 0.15SnS$_2$/BiVO$_4$ photocatalyst for the photocatalytic degradation of CIP up to five cycles, which shows a similar type degradation pattern in each cycle, reflecting the photocatalyst's high stability. The excellent structural stability of the 0.15SnS$_2$/BiVO$_4$ photocatalyst was further confirmed by the unchanged XRD pattern (Table S3) and morphology of pristine and used photocatalyst (Fig. 7b-c). Further, the toxicity level of the used 0.15SnS$_2$/BiVO$_4$ photocatalyst was accessed by the amount of leached metal species, i.e., Bi, V, and Sn, using the ICP-OES technique. The respective calibration plots of Bi, V, Sn, and S were used to determine the amount of leached concentration (Fig. S2 of Supporting Information). It is observed that the leaching concentrations correspond to ~ 0.93% Bi (306 µg/L), 1.5% V (295.12 µg/L), and 0.8% Sn (285.32 µg/L) of the total weight of the catalyst, which is well within the permissible limits (Table S4).
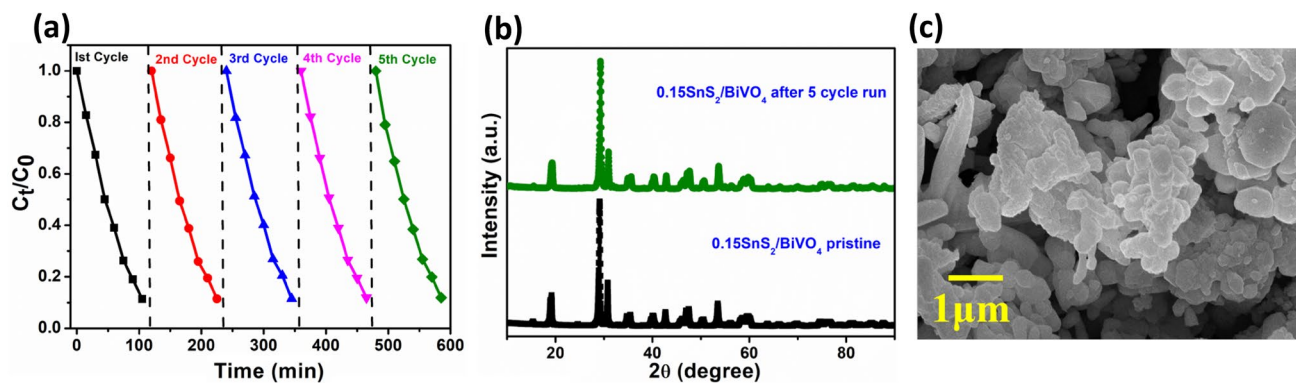
Fig. 7 **a** Recyclability experiment; **b** XRD and **c** FESEM image of the recycled photocatalyst

3.8 Photocatalytic Mechanism

The photoluminescence spectra of $BiVO_4$, $0.10SnS_2/BiVO_4$, $0.15SnS_2/BiVO_4$, and $0.20SnS_2/BiVO_4$ nanocomposite exhibit broad spectra with a peak at a wavelength of ~514 nm. From Fig. 8a, it is clearly visible that $BiVO_4$ owns a strong PL emission peak at ~514 nm, while the emission peaks of the $SnS_2/BiVO_4$ nanocomposites show a decrease in PL intensity as compared to that of $BiVO_4$. These results indicated that the recombination of charge carriers is strongly suppressed in $SnS_2/BiVO_4$, and it favoured

the interfacial charge transfer in $SnS_2/BiVO_4$ because of heterojunction formation. These separated charge carriers move to the surface and react with the molecular oxygen and water to form reactive oxygen species (ROS) [44]. To verify the efficient charge transfer of SnS_2, $BiVO_4$ and $0.15SnS_2/BiVO_4$ nanocomposites, the photocurrent, and EIS characterizations of SnS_2, $BiVO_4$, and $0.15SnS_2/BiVO_4$ nanocomposite were performed and results are shown in Fig. 8b-c respectively. The SnS_2 and $BiVO_4$ exhibits a low photocurrent attributing to heavily charge recombination. However, the photocurrent performance of $0.15SnS_2/BiVO_4$ NCs was

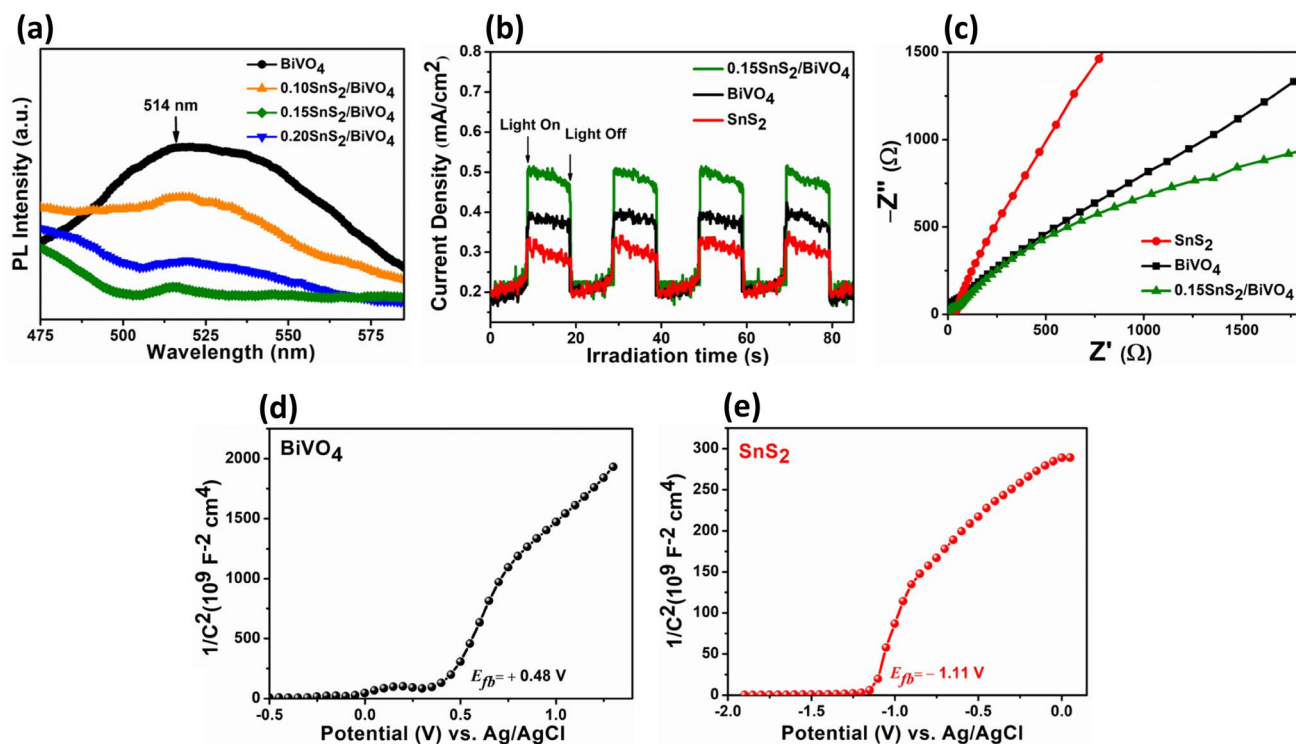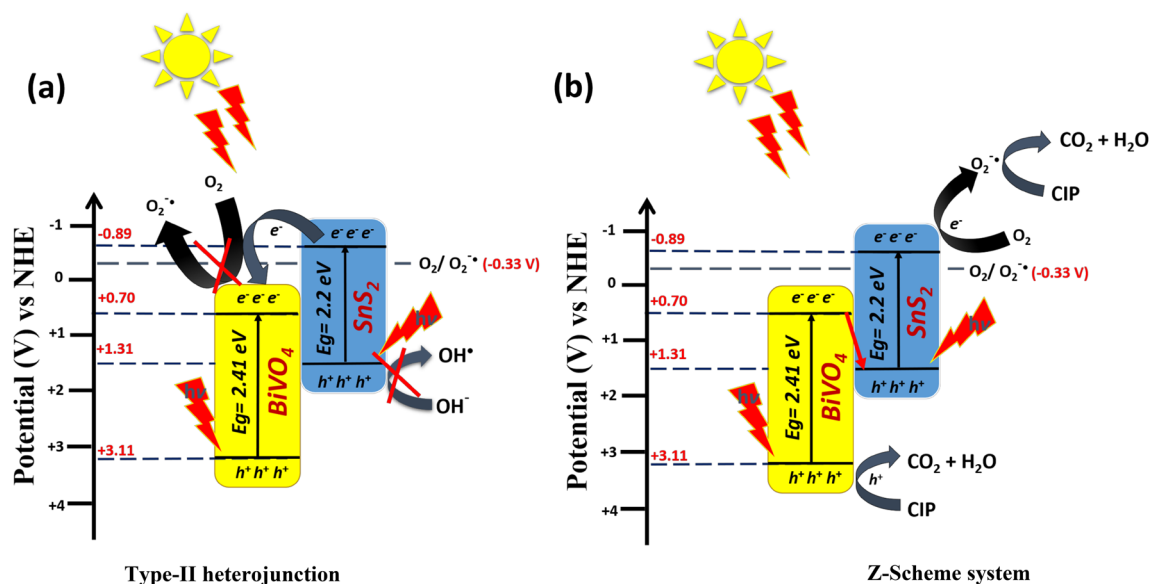**Fig. 8** **a** PL spectra of $BiVO_4$, $0.10SnS_2/BiVO_4$ NCs, $0.15SnS_2/BiVO_4$ NCs, and $0.20SnS_2/BiVO_4$ NCs, **b** photocurrent, **c** EIS of $BiVO_4$, SnS_2 and $0.15SnS_2/BiVO_4$ and, **c-d** Mott-Schottky plot of $BiVO_4$ and SnS_2

Scheme 1 Possible photocatalytic degradation mechanism ofCIP over $SnS_2/BiVO_4$ nanocomposite under sunlightirradiation (**a**) traditional type-II heterojunction, (**b**) Z-scheme type

higher than individual components SnS_2 and $BiVO_4$, which demonstrates that the $0.15SnS_2/BiVO_4$ can separate electron-hole pairs more effectively. The charge carrier mobility of $BiVO_4$, SnS_2, and $SnS_2/BiVO_4$ nanocomposite was further evaluated by EIS Nyquist plot (Fig. 8c). The radius of the impedance arc for $0.15SnS_2/BiVO_4$ was minimum as compared to that of $BiVO_4$ and SnS_2 (Fig. 8c). Smaller impedance arc of $0.15SnS_2/BiVO_4$, attributed to high electron-hole separation or high interface charge transfer [45]. Therefore, the rapid charge separation and the transport of charge carriers in $0.15SnS_2/BiVO_4$ result in enhanced photocatalytic performance [46, 47].

In this work, a Mott–Schottky experiment was performed to determine the positions of the E_{CB} and E_{VB} of SnS_2 and $BiVO_4$, and to analyze the charge transfer route. The Mott-Schottky curve can be obtained by using the equation (Section S3) and plotting $1/Cs^2$-E with potential corresponding to $1/Cs^2$ [48]. As shown in Fig. 8d-e, for SnS_2 and $BiVO_4$, the intercepts of the linear region and X-axis is -1.11 V and $+0.48$ V (vs. Ag/AgCl), respectively [49]. Therefore, the E_{CB} of SnS_2 and $BiVO_4$ will be -0.89 V and $+0.70$ V vs. NHE, respectively. Meanwhile, the E_{VB} of SnS_2 and $BiVO_4$ is $+1.31$ V and $+3.11$ V vs. NHE respectively.

As the E_{CB} of SnS_2 shows more negative potential than $BiVO_4$, the electron from the E_{CB} of SnS_2 migrates to the E_{VB} of $BiVO_4$, according to the type-II heterojunction system. In this type of charge transfer mode, the electron present in the E_{CB} of $BiVO_4$ could not reduce O_2 into a superoxide radical anion ($O_2^{-\bullet}$) because the E_{CB} of $BiVO_4$ has more positive potential than that of the superoxide radical anion ($O_2^{-\bullet}$, -0.33 eV vs. N.H.E) [50]. Thus, the electron migration in

type-II heterojunction is not favorable for producing the superoxide radical anion, which is the main reactive oxygen species responsible for the degradation of CIP, according to the radical trapping experiment (Scheme 1b). Based on the above characterization results, a possible Z-scheme mechanism for the degradation of antibiotics using $SnS_2/BiVO_4$ heterojunction photocatalyst was proposed, as shown in scheme-1a-b. Under sunlight irradiation, both SnS_2 and $BiVO_4$ absorb visible light photons to produce photogenerated e^- and h^+. In $SnS_2/BiVO_4$ heterojunction, the photogenerated e^- in the E_{CB} of $BiVO_4$ (e_{CB}^-) would migrate to E_{VB} of SnS_2 to recombine immediately with the photogenerated holes (h_{VB}^+), while the E_{VB} holes of $BiVO_4$ remain on it to oxidize CIP directly. In addition, the e^- in the E_{CB} of SnS_2 could easily migrate to the O_2 molecules adsorbed on the surface $SnS_2/BiVO_4$ heterojunctions to produce the strong oxidant i.e., superoxide radicals that oxidize CIP. The photogenerated charge carrier transfer process can be described as:

4 Conclusion

A Z-scheme $SnS_2/BiVO_4$ heterogeneous photocatalyst with excellent photocatalytic efficiency towards CIP degradation under natural sunlight was synthesized by in-situ hydrothermal method. The apparent rate constant for CIP photocatalytic degradation by $0.15SnS_2/BiVO_4$ photocatalyst was about 4.83 times and 6.41 times higher than that of the $BiVO_4$ photocatalyst. The enhanced photocatalytic performance is attributed to the improved visible light response

and efficient charge separation due to the formation of a Z-scheme heterojunction. The excellent re-usability and chemical stability of $SnS_2/BiVO_4$ nanocomposite make it an effective photocatalyst for the removal of antibiotics from wastewater.

Author Contributions GK contributed to conception and design experiments, data analysis and preparation of manuscript.

Data Availability All the datasets used and/or analyzed in this study are available in the manuscript and supplementary information can be asked from the corresponding author upon request.

Declarations

Competing Interests The authors declare no competing interests.

Ethical Approval Not applicable.

consent to Participate Not applicable.

Consent for Publication Not applicable.

References

1. R. Singh, A.P. Singh, S. Kumar, B.S. Giri, K.H. Kim, J. Clean. Prod. **234**, 1484 (2019)
2. J. Rivera-Utrilla, M. Sánchez-Polo, M.Ã. Ferro-García, G. Prados-Joya, R. Ocampo-Pérez, Chemosphere **93**, 1268 (2013)
3. J. Wang, R. Zhuan, Sci. Total Environ. **701**, 135023 (2020)
4. S. Sharma, A. Bhattacharya, Appl. Water Sci. **7**, 1043 (2017)
5. S. Manzetti, R. Ghisi, Mar. Pollut Bull. **79**, 7 (2014)
6. R. Zhang, J. Tang, J. Li, Z. Cheng, C. Chaemfa, D. Liu, Q. Zheng, M. Song, C. Luo, G. Zhang, Sci. Total Environ. **197**, 450–451 (2013)
7. J. Fick, H. Söderström, R.H. Lindberg, C. Phan, M. Tysklind, D.G.J. Larsson, Environ. Toxicol. Chem. **28**, 2522 (2009)
8. M.Z. Akbari, Y. Xu, Z. Lu, L. Peng, Environ. Adv. **5**, 100111 (2021)
9. N.A. Khan, S. Ahmed, I.H. Farooqi, I. Ali, V. Vambol, F. Changani, M. Yousefi, S. Vambol, S.U. Khan, A.H. Khan, TrAC-Trends Anal. Chem (2020). https://doi.org/10.1016/j.trac.2020.115921
10. C. Adams, Y. Wang, K. Loftin, M. Meyer, J. Environ. Eng. **128**, 253 (2002)
11. I. Michael, L. Rizzo, C.S. McArdell, C.M. Manaia, C. Merlin, T. Schwartz, C. Dagot, D. Fatta-Kassinos, Water Res. **47**, 957 (2013)
12. Q.T. Dinh, E. Moreau-Guigon, P. Labadie, F. Alliot, M.J. Teil, M. Blanchard, M. Chevreuil, Chemosphere. **168**, 483 (2017)
13. M.J.F. Calvete, G. Piccirillo, C.S. Vinagreiro, M.M. Pereira, Coord. Chem. Rev. **395**, 63 (2019)
14. J.C. Durán-Álvarez, E. Avella, R.M. Ramírez-Zamora, R. Zanella, Catal. Today. **266**, 175 (2016)
15. Y. Wang, K. Ding, R. Xu, D. Yu, W. Wang, P. Gao, B. Liu, J. Clean. Prod. (2020). https://doi.org/10.1016/j.jclepro.2019.119108
16. R. Yang, Z. Zhu, C. Hu, S. Zhong, L. Zhang, B. Liu, W. Wang, Chem. Eng. J. **390**, 124522 (2020)
17. Y. Wang, D. Yu, W. Wang, P. Gao, S. Zhong, L. Zhang, Q. Zhao, B. Liu, Sep. Purif. Technol. **239**, 116562 (2020)
18. N. Wetchakun, S. Chaiwichain, B. Inceesungvorn, K. Pingmuang, S. Phanichphant, A.I. Minett, J. Chen (2012). https://doi.org/10.1021/am300812n
19. C. Lai, M. Zhang, B. Li, D. Huang, G. Zeng, Chem. Eng. J. **358**, 891 (2019)
20. M. Yan, Y. Wu, Y. Yan, X. Yan, F. Zhu, Y. Hua, W. Shi, ACS Sustain Chem. Eng **4**(3), 757–766 (2016)
21. T. Soltani, A. Tayyebi, B. Lee, J. Environ. Manage. **232**, 713 (2019)
22. Y. Deng, L. Tang, C. Feng, G. Zeng, J. Wang, Y. Zhou, Y. Liu, B. Peng, H. Feng, J. Hazard. Mater. **344**, 758 (2018)
23. M. Ge, L. Liu, Z. Zhou, CrystEngComm **14**(3), 1038–1044 (2012)
24. A. Raja, P. Rajasekaran, K. Selvakumar, M. Arunpandian, K. Kaviyarasu, S.A. Bahadur, M. Swaminathan, Sep. Purif. Technol. **233**, 115996 (2020). https://doi.org/10.1016/j.seppur.2019.115996
25. W. Yin, W. Wang, L. Zhou, S. Sun, L. Zhang, J. Hazardous Mater. **173**(1–3), 194–199 (2010)
26. Q. Tang, X. Luo, S. Yang, Y. Xu, Sep. Purif. Technol. **248**, 117039 (2020)
27. H. Li, K. Yu, X. Lei, B. Guo, H. Fu, Z. Zhu, J. Phys. Chem. **119**(39), 22681–22689 (2015)
28. X. Chen, J. Zhou, Y. Chen, Y. Zhou, L. Ding, H. Liang, X. Li, Process Safety Environ. Protect **145**, 364–377 (2021)
29. H. Jiang, H. Endo, H. Natori, M. Nagai, K. Kobayashi, Mater. Res. Bulletin **44**(3), 700–706 (2009)
30. M. Long, W. Cai, J. Cai, B. Zhou, X. Chai, Y. Wu, J. Phys. Chem. **110**(41), 20211–20216 (2006)
31. Z. Qiang, X. Liu, F. Li, T. Li, M. Zhang, H. Singh, M. Huttula, W. Cao, Chem. Eng. J. **403**, 126327 (2021)
32. J. Sun, C.H. Shen, J. Guo, H. Guo, Y.F. Yin, X.J. Xu, Z.H. Fei, Z.T. Liu, X.J. Wen, J. Colloid Interface Sci. **588**, 19 (2021)
33. J. Mao, B. Hong, J. Wei, J. Xu, Y. Han, H. Jin, D. Jin, X. Peng, J. Li, Y. Yang, J. Gong, H. Ge, X. Wang, ChemistrySelect **4**, 13716 (2019)
34. X. Luo, Z. Chen, S. Yang, Y. Xu, J. Colloid Interface Sci. **532**, 456 (2018)
35. S. Chen, D. Huang, G. Zeng, W. Xue, L. Lei, P. Xu, Chem. Eng. J. **382**, 122840 (2020)
36. S. Singla, S. Basu, P. Devi, J. Ind. Eng. Chem. **118**, 119 (2023)
37. Y. Li, X. Wang, L. Gao, J. Mater. Sci. Mater. Electron. **30**, 16015 (2019)
38. X. Gao, G. Huang, H. Gao, C. Pan, H. Wang, J. Yan, Y. Liu, H. Qiu, N. Ma, J. Gao, J. Alloys Compd. **674**, 98 (2016)
39. G. Kumar, R.K. Dutta, J. Phys. Chem. Solids. **164**, 110639 (2022)
40. J. Tauc, R. Grigorovici, A. Vancu, Phys. Status Solidi. **15**, 627 (1966)
41. G.K.I. Mukherjee, M.D.B.P. Vellenki, Int. J. Environ. Sci. Technol. **20**, 2903 (2022)
42. G. Kumar, V. Cilamkoti, R.K. Dutta, Colloids Surf. Physicochem Eng Asp. **639**, 128368 (2022)
43. G. Kumar, J. Kumar, M. Bag, R. Kumar, Dutta, Sep. Purif. Technol. **292**, 121040 (2022)
44. G. Kumar, R. Kumar, Environ. Sci. Pollut Res. **29**, 57758 (2022)
45. K. Bisht, G. Kumar, R.K. Dutta, Ind. Eng. Chem. Res. **61**(46), 16946–16961 (2022)

46. Z. Li, X. Meng, Z. Zhang, Catal. Today. **315**, 67 (2018)
47. J. Yi, H. Mo, B. Zhang, J. Song, D. Liu, G. Zhuo, Sep. Purif. Technol. **211**, 474 (2019)
48. F. Deng, Y. Luo, H. Li, B. Xia, X. Luo, S. Luo, D.D. Dionysiou, J. Hazard. Mater. **383**, 121127 (2020)
49. Q. Zhou, W. Huang, C. Xu, X. Liu, K. Yang, D. Li, Y. Hou, D.D. Dionysiou, Chem. Eng. J. **420**, 129582 (2021)
50. G. Kumar, R.K. Dutta, Process. Saf. Environ. Prot. **159**, 862 (2022)